

# DO ARCS REQUIRE FLAT HALO CUSPS?

MATTHIAS BARTELMANN<sup>1</sup>, MASSIMO MENEGHETTI<sup>2</sup>

<sup>1</sup> ITA, UNIVERSITÄT HEIDELBERG, TIERGARTENSTR. 15, D-69121 HEIDELBERG, GERMANY

<sup>2</sup> DIPARTIMENTO DI ASTRONOMIA, UNIVERSITÀ DI PADOVA, VICOLO DELL'OSSERVATORIO 5, I-35122 PADOVA, ITALY

November 1, 2018

## ABSTRACT

It was recently claimed that several galaxy clusters containing radial and tangential gravitational arcs and having a measured velocity-dispersion profile for the brightest cluster galaxy had to have central density profiles considerably flatter than those found in CDM cluster simulations. Using a simple analytic mass model, we confirm this result for axially symmetric mass distributions, but show that steep density profiles are well in agreement with the cluster requiring the flattest axially symmetric profile once even small deviations from axial symmetry are introduced.

## 1. INTRODUCTION

Are observed gravitational arcs in galaxy clusters compatible with the density profiles produced in CDM simulations, which consistently find that the dark-matter density increases towards halo centres as  $r^{-1}$  or steeper? Building upon a suggestion by Miralda-Escudé (1995), Sand et al. (2003, hereafter STSE) have recently analysed six galaxy clusters containing tangential arcs, three of which also contain radial arcs. Apart from the lensing data, the method uses constraints on the mass profile derived from the dynamics of the central cluster galaxies, specifically from its velocity dispersion profile (see also Sand et al. 2002).

The method sets strong constraints. In a cluster showing both radial and tangential arcs, the velocity dispersion measurement essentially fixes the mass divided by the radius. Radial arcs constrain the slope of the projected mass profile at their location, and tangential arcs constrain the total mass enclosed by their radial distance from the cluster centre.

Using this technique, STSE find that their sample of six clusters is incompatible with dark-matter density profiles proportional to  $r^{-1}$  or steeper, but consistently require profiles as flat as  $r^{-0.5}$ .

If true, this result would be of great importance for CDM because such flat profiles are not found in simulations. However, the analysis by STSE is based on the assumption of axial symmetry. We re-analyse their constraints here for the cluster Abell 383, which is the one apparently requiring the most significant discrepancy between simulated CDM density profiles. In doing so, we describe the lens model and its parameters in Sect. 2 and illustrate the basic reason why the method strongly prefers a shallow central density profile. Next, we introduce ellipticity in Sect. 3 and illustrate its substantial impact. We conclude in Sect. 4 that even moderate ellipticity can easily remove the discrepancy between the lensing observations in Abell 383 and the typical CDM halo profiles.

Like STSE, we use a  $\Lambda$ CDM cosmological model with matter density  $\Omega_0 = 0.3$ , cosmological constant  $\Omega_\Lambda = 0.7$ , and Hubble constant  $H_0 = 65 \text{ km s}^{-1} \text{ Mpc}^{-1}$ .

## 2. LENS MODEL

Our lens model is adapted from STSE. It consists of a model for the dark-matter halo,

$$\rho_h(x) = \frac{\rho_s}{x^\beta(1+x)^{3-\beta}}, \quad (1)$$

which is the profile found by Navarro et al. (1997) for  $\beta = 1$ . Steeper profiles with  $\beta \rightarrow 1.5$  are found by several other groups, among them Moore et al. (1998); Jing & Suto (2000); Klypin et al. (2001). The radial coordinate  $x = r/r_s$  is the physical radius divided by a scale radius  $r_s$ , which STSE assume to be  $r_s = 400 \text{ kpc}$ . We adopt this value because the results are insensitive to it.

In addition, the brightest cluster galaxy, assumed to be concentric with the cluster, adds matter density to the cluster centre. Following the light profile, it is assumed to have a Jaffe (1983) density profile,

$$\rho_g(\bar{x}) = \frac{\rho_J}{\bar{x}^2(1+\bar{x})^2}, \quad (2)$$

where now  $\bar{x} = r/r_J$  is the radius in units of the Jaffe radius  $r_J$ . Fitting to the light profile of the brightest cluster galaxy, STSE find  $r_J = r_e/0.76$ , where  $r_e$  is the usual effective radius of an  $r^{1/4}$  surface-brightness profile. For Abell 383,  $r_e = 46.75 \pm 2.04 \text{ kpc}$ .

Lensing properties are straightforwardly derived from these density profiles. The convergence  $\kappa$  for the dark-matter halo is

$$\kappa_h(x) = 2 \kappa_s x^{1-\beta} \int_0^{\pi/2} \frac{\sin \theta d\theta}{(x + \sin \theta)^{3-\beta}} \quad (3)$$

(Wyithe et al., 2001); the special case for the NFW profile,  $\beta = 1$ , was derived in Bartelmann (1996). The factor  $\kappa_s$  is defined by

$$\kappa_s \equiv \rho_s r_s \Sigma_{\text{cr}}^{-1}, \quad (4)$$

with the usual critical surface-mass density for lensing  $\Sigma_{\text{cr}}$ . For the Jaffe profile,

$$\kappa_g = \kappa_J \left[ \frac{\pi}{x} + \frac{2}{1-x^2} \left( 1 - \frac{2-x^2}{\sqrt{1-x^2}} \text{acosh} \frac{1}{x} \right) \right], \quad (5)$$

(Jaffe, 1983), with  $\kappa_J \equiv \rho_J r_J \Sigma_{\text{cr}}^{-1}$ . Deflection angles are derived from

$$\alpha(x) = \frac{2}{x} \int_0^x y \kappa(y) dy. \quad (6)$$

This needs to be computed numerically for the dark-matter profile, while

$$\alpha_J(x) = \kappa_J \left[ \pi - \frac{2x \text{acosh}(x^{-1})}{\sqrt{1-x^2}} \right] \quad (7)$$

for the Jaffe profile. Given the deflection-angle profile  $\alpha(x)$ , the radial and tangential eigenvalues are

$$\lambda_r(x) = 1 - \frac{d\alpha(x)}{dx}, \quad \lambda_t(x) = 1 - \frac{\alpha(x)}{x}, \quad (8)$$

TABLE 1.—Fixed parameters assumed for the lensing analysis in this paper, taken from STSE. The two remaining parameters, i.e. the density profile slope  $\beta$  and the ratio of masses  $\mu$  contributed by the dark-matter and galaxy density profiles contained within the Jaffe radius, are taken as free parameters.

lens redshift	$z_d$	0.189
source redshift	$z_s$	1.01
effective radius	$r_e$	46.75 kpc
velocity dispersion	$\sigma_v$	250 km s <sup>-1</sup>

respectively (see, e.g., Schneider et al. 1992; Narayan & Bartelmann 1999). Radial or tangential critical curves are found where  $\lambda_r = 0$  or  $\lambda_t = 0$ . A useful relation for axially symmetric lens models is

$$\lambda_r(x) = 2\kappa(x) - \frac{\alpha(x)}{x}. \quad (9)$$

In our application, source and lens redshifts together with the cosmological model fix the critical surface-mass density  $\Sigma_{\text{cr}}$ . The Jaffe radius  $r_j$  is fixed by fitting the surface-brightness profile. The mass of the brightest cluster galaxy is determined by the central velocity dispersion as described below. The scale radius of the dark-matter profile is kept fixed at  $r_s = 400$  kpc. The only remaining parameter is the dark-matter density scale  $\rho_s$ , which we express by the ratio  $\mu$  between the masses contributed by the cluster- and galaxy density profiles within the Jaffe radius. This ratio will effectively scale the cluster mass relative to the fixed galaxy mass.

The circular velocity for an spherically symmetric density profile is

$$v_{\text{rot}}^2 = \frac{GM(r)}{r}. \quad (10)$$

For the dark-matter profile,  $M(r)$  is steeper than  $r$ , hence  $v_{\text{rot}} \rightarrow 0$  for  $r \rightarrow 0$  in the dark-matter profile only. Thus, the measured circular velocity near the centre of the brightest cluster galaxy must be dominated by the galaxy itself. Well within the Jaffe radius, the Jaffe profile is isothermal with  $\rho_g \propto r^{-2}$ . Thus, the velocity dispersion profile is expected to be flat close to the cluster centre, and the velocity dispersion is approximately related to the circular velocity by

$$\sigma_v = \sqrt{2} v_{\text{rot}}. \quad (11)$$

Through Eqs. (10) and (11), the central velocity dispersion thus fixes the mass contained in the Jaffe profile. The assumed mass ratio between the masses of the dark halo and the galaxy profile, and the central slope  $\beta$  of the dark-matter density profile, thus completely determine the total density profile composed of a galaxy- and a dark-matter profile.

Specifically, aiming at the cluster Abell 383 which produced the most significant deviation from the numerically simulated dark-matter profiles in the study by STSE, we adopt the fixed parameters listed in Tab. 1.

The convergence, deflection-angle and radial and tangential eigenvalue profiles  $\kappa(x)$ ,  $\alpha(x)$ ,  $|\lambda_r(x)|$  and  $|\lambda_t(x)|$  are displayed in Fig. 1 for  $\beta = 0.5$  and mass ratio  $\mu = 60$ . The figure illustrates that the (projected) density profile near the cluster centre is dominated by the near-isothermal slope of the brightest cluster galaxy. Near the Jaffe radius, it flattens towards the central slope of the dark-matter density profile, and then steepens towards  $\kappa \propto x^{-2}$  as  $x$  approaches unity. Interestingly, the radial eigenvalue profile has two roots, indicating the presence of two

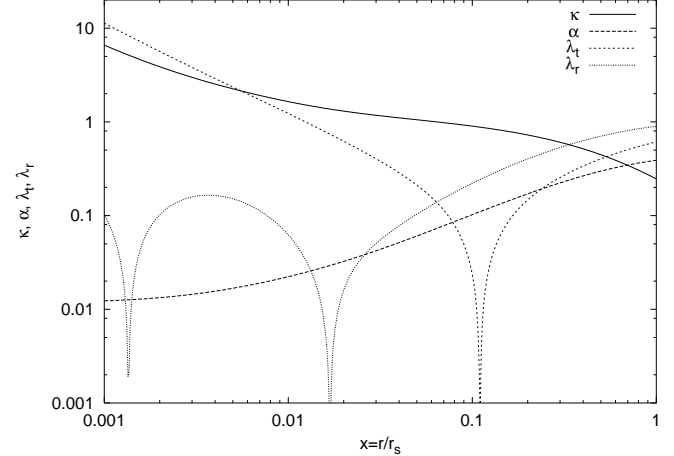


FIG. 1.—Radial profiles are shown for the lensing convergence  $\kappa$ , the deflection angle  $\alpha$ , and the tangential and radial eigenvalues of the lens mapping  $\lambda_t$  and  $\lambda_r$ , respectively. The lens model is axially symmetric and composed of a central Jaffe profile and a dark matter profile with a central slope of  $-\beta = -0.5$ .

radial critical curves. For Abell 383, the inner radial critical curve is too close to the cluster centre for having any practical relevance, but clusters at more favourable redshifts might show signatures of a double radial critical curve. This is an interesting feature of the combination of a steep, near-isothermal galaxy profile embedded into a relatively flat dark-matter halo.

Having defined the axially symmetric lens model, the constraints imposed by the central velocity dispersion, the radial and the tangential arcs are straightforwardly understood. As mentioned before, the central velocity dispersion is almost exclusively contributed by the mass associated with the brightest cluster galaxy because  $M/r$  tends to zero for  $r \rightarrow 0$  for the flatter dark-matter density profile. In contrast, the tangential arc is located at a radius which encloses a mean surface-mass density of unity. A first constraint thus derives from the requirement to have the central cluster mass dominated by the brightest cluster galaxy, and yet to have sufficient mass in the dark-matter halo to produce tangential arcs at relatively large cluster-centric radii. In the axially symmetric models, this is achieved by flattening the dark-matter density profile.

A second constraint is imposed by the radial critical curve, where the derivative of the deflection angle reaches unity. For the Jaffe profile alone, the deflection angle is flat. It steepens as the total density profile becomes flatter at radii where the dark matter starts dominating, then flattens again as the cluster-centric radius approaches the scale radius of the dark-matter profile. If the dark-matter density profile is relatively flat, the increase of the deflection-angle slope occurs closer to the brightest cluster galaxy than for a steeper dark-matter profile. The second constraint thus derives from the requirement of having a radial arc rather close to the brightest cluster galaxy, while the first constraint requires a tangential arc rather far away from the cluster centre.

Figure 2 illustrates the situation. The abscissa is the mass ratio between dark and luminous constituents within the Jaffe radius. The ordinate is the cluster-centric radius in kpc. The horizontal bars mark the radial and tangential arc locations in Abell 383 with their respective uncertainties. The curves in the upper and lower halves of the figure show the tangential and radial critical radii, respectively, for dark-matter profiles with four different central slopes,  $\beta \in \{0.25, 0.5, 0.75, 1.0\}$ , as marked in the plot.

A model can explain both the radial and the tangential arc if

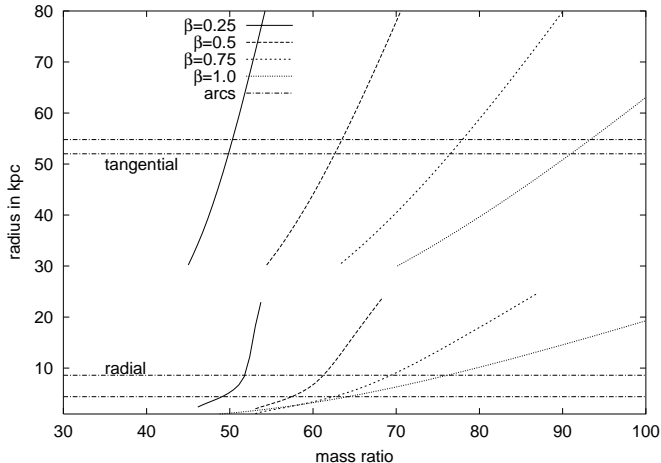


FIG. 2.—Illustration of the radial and tangential critical radii for an axially symmetric lens model composed of a central Jaffe profile and a dark matter profile with four different values for the central slope,  $\beta = \{0.25, 0.5, 0.75, 1.0\}$ , respectively, as indicated in the plot. The abscissa shows the mass ratio between the cluster component and the galaxy component within the Jaffe radius, the ordinate is the cluster-centric radius in kpc. The two horizontal stripes mark the locations of the radial and tangential arcs, as labelled. The curves in the upper and lower halves of the plot mark the tangential and radial critical radii, respectively.

there is a single mass ratio for which the radial critical curve falls into the lower horizontal band, and the tangential critical curve falls into the upper horizontal band. Figure 2 confirms the result by STSE regarding Abell 383. Only for shallow central density profiles,  $\beta \sim 0.5$ , can the position of both the tangential and the radial arc be understood. For a mass ratio near 60, the lens model has radial and tangential critical curves in the observed ranges. Steeper mass profiles, e.g. the NFW model with  $\beta = 1$ , either have the tangential arc in the right range if the mass ratio is  $\sim 90$ , but then the radial arc is too distant from the cluster centre, or the radial arc location is reproduced if the mass ratio is  $\sim 70$ , but then the tangential arc is way too close to the cluster centre. The core of the problem is thus that the location of the radial arc requires a relatively low cluster mass, and then a steep mass profile forces the tangential arc too close to the cluster centre.

### 3. ELLIPTICITY

#### 3.1. Model and numerical results

These conclusions are valid for axially symmetric lens models. As we shall show now, the situation changes considerably if deviations from axial symmetry are allowed.

As a simple model for asymmetry, we deform the lens model such that iso-contour lines of the lensing potential  $\psi$  are ellipses. We thus introduce the radial coordinate

$$\bar{x} = \left[ (1 - \epsilon)x_1^2 + \frac{x_2^2}{1 - \epsilon} \right]^{1/2} \quad (12)$$

and replace  $\psi(x)$  by  $\psi(\bar{x})$ . Being the gradient of  $\psi$ , the deflection angle  $\bar{\alpha}$  now has the components

$$\alpha_1(x_1, x_2) = \frac{\alpha(\bar{x})x_1}{\bar{x}}(1 - \epsilon), \quad \alpha_2(x_1, x_2) = \frac{\alpha(\bar{x})x_2}{(1 - \epsilon)\bar{x}}, \quad (13)$$

where  $\alpha(\bar{x})$  is the deflection-angle profile of the axially symmetric lens taken at  $\bar{x}$ . The axially symmetric case is recovered for  $\epsilon = 0$ .

Elliptical distortions of the lensing potential lead to dumbbell-shaped surface-mass distributions if  $\epsilon$  becomes large,  $\epsilon \gtrsim 0.2$  day, depending on the density profile. This is certainly unwanted for galaxy-sized lenses, but not necessarily for cluster lenses which are often highly structured. In any case, we shall see below that the impact of a small ellipticity  $\epsilon \ll 1$  on the location of the critical curves is identical for lenses with elliptical iso-potential curves and axially symmetric lenses embedded into external shear.

Ellipticity stretches the tangential critical curves along the major axis of the ellipse and shrinks it along the minor axis, and deforms the radial critical curve in the perpendicular direction. This implies that the cluster-centric distance of the critical curves now covers a range of radii. This range is surprisingly wide even for small ellipticities, as Fig. 3 illustrates.

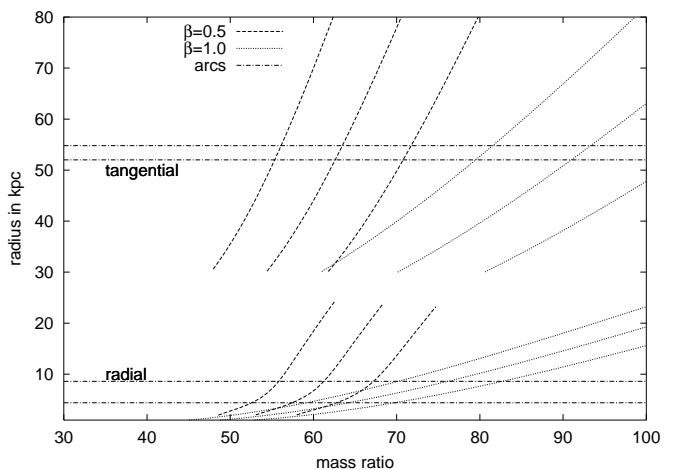


FIG. 3.—Changes in the location of the radial and tangential critical curves in response to a moderate elliptical distortion of the lensing potential. The figure is arranged to resemble Fig. 2, but showing results for  $\beta = 0.5$  and  $\beta = 1.0$  only for clarity. Three curves are shown for each profile slope. The central curve shows the critical radius for axial symmetry, the other two curves indicate the range of radii of the critical curves for an ellipticity parameter of  $\epsilon = 0.1$ . Even moderate ellipticity widens the radial ranges such that the observed radial and tangential critical radii can quite easily be reached even for steep profiles.

The figure is arranged in the same way as Fig. 2 and also specialised for the cluster Abell 383. The radius from the cluster centre is plotted against the mass ratio between cluster and brightest cluster galaxy for different central slopes  $\beta$  of the cluster density profile. The observed locations of the tangential and radial arcs are marked as horizontal bars. For clarity, we now show results for two values of  $\beta$  only,  $\beta \in \{0.5, 1\}$ , but illustrate with three curves for each  $\beta$  the radial range covered by the tangential and radial critical curves for a small ellipticity parameter  $\epsilon = 0.1$ . For a fixed mass ratio, the radial range is given by the vertical distance between the top and bottom curves of the same type. Conversely, for a fixed radius, the horizontal distance between the left and right curves of the same type show the range of mass ratios for which arcs at that radius can be produced somewhere along the respective critical curves. The central curves reproduce the critical radii for the axially symmetric case.

Evidently, the impact of the small ellipticity  $\epsilon$  on the location of the critical curves is quite large. For the shallow profile,  $\beta = 0.5$ , and a mass ratio of 60, the tangential critical radius ranges from 27 to 70 kpc, while the axially symmetric result is 45. For the same mass ratio and density-profile slope of  $\beta = 0.5$ , the radial critical radius ranges between 3 and 19 kpc around the

axially-symmetric value of 7 kpc. Thus, even the low ellipticity of  $\epsilon = 0.1$  makes the location of the tangential and radial critical curves vary by about a factor of 1.5 and more than a factor of two, respectively, around the cluster. Interestingly, the radial ranges for tangential and radial critical curves now overlap even for the steep profile with  $\beta = 1$ . For a mass ratio of  $\sim 80$ , the observed positions of both the radial and the tangential arcs fall within the ranges allowed by the model.

### 3.2. Analytic description

These results can be reproduced analytically. For coordinate axes aligned with the elliptical iso-potential contours, the minimum and maximum values of the critical radii occur on the axes. The intersection of the tangential critical curve with the  $x_1$ -axis satisfies

$$1 - \frac{\alpha(\bar{x})}{(1-\epsilon)\bar{x}} = 0. \quad (14)$$

Expanding around the solution for the critical radius in the axially symmetric case, which satisfies

$$1 - \frac{\alpha(x)}{x} = 0, \quad (15)$$

and assuming  $\epsilon \ll 1$ , we find the amount  $\delta x$  by which the tangential critical curve is shifted on the  $x_1$ -axis relative to the axially symmetric critical radius. Repeating the calculation for the  $x_2$  axis, we obtain

$$\delta x_t = \pm \frac{\epsilon x}{2(\kappa_t - 1)} \quad (16)$$

where the  $+$  and  $-$  signs apply to the  $x_1$  and  $x_2$  axes, respectively, and  $\kappa_t$  is the convergence at the tangential critical radius of the axially symmetric model. Repeating this analysis for the radial critical curve yields

$$\delta x_r = \pm \frac{\epsilon x}{2(\kappa_r - 1 + \kappa'_r x)}, \quad (17)$$

where  $\kappa_r$  and  $\kappa'_r$  are the convergence and its radial derivative at the radial critical radius of the unperturbed lens model. Figure 4 shows the relative shifts for unit ellipticity, i.e.  $\delta x_{t,r}/(\epsilon x)$ , for the two central slopes  $\beta \in \{0.5, 1\}$ .

The figure shows that, for a mass ratio of 60 and a central density slope of  $\beta = 0.5$ , the relative shifts for  $\epsilon = 0.1$  are of order 100% for the radial critical curve, and 40% for the tangential critical curve, confirming the numerical results illustrated in Fig. 3. For the steeper profile with  $\beta = 1$ , the respective relative changes are of order 40% and 20% for the same mass ratio and ellipticity.

It is straightforward to show that the first-order results (16) and (17) remain valid if the lens model is not itself deformed, but embedded into an external shear  $\gamma$ . In that case,  $\gamma$  simply replaces  $\epsilon$  in these equations which are otherwise unchanged.

Equations (16) and (17) show that the amount by which ellipticity or shear shift the critical curves depends highly sensitively on the slope of the convergence profile  $\kappa(x)$ . For a singular isothermal sphere, for instance,  $\kappa = 0.5$  at the location of the tangential critical curve, which is at  $x = 1$ . Thus,  $\delta_t = \pm \epsilon$  in this case. Flatter profiles, however, have  $\kappa$  closer to unity in Eq. (16) because the tangential critical radius encloses a mean convergence of unity. The relative shift of the tangential critical curve is thus amplified for flatter density profiles, as illustrated in Fig. 4 for the two choices of  $\beta$ . As the figure also shows, the situation is more extreme for the radial critical curve. Flatter profiles thus much more sensitive to external shear or internal ellipticity than steeper profiles.

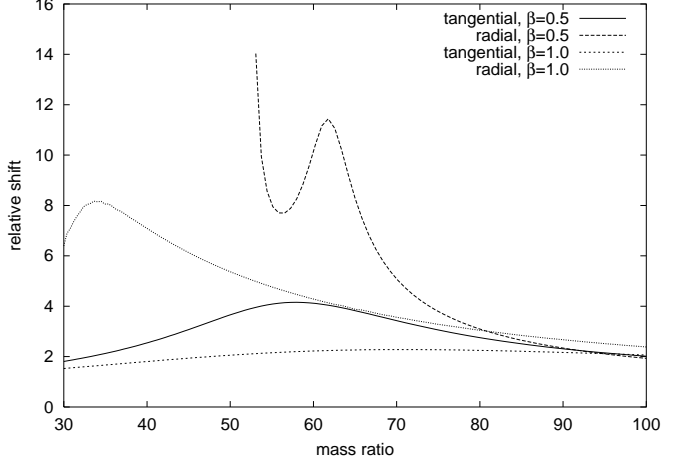


FIG. 4.—Relative shift per unit ellipticity,  $\delta x/(\epsilon x)$ , of the radial and tangential critical curves caused by external shear or internal ellipticity. Results for two values of the central density-profile slope  $\beta$  are shown. For example, for a mass ratio of 60,  $\beta = 0.5$  and  $\epsilon = 0.1$ , the radial critical curve shifts by  $\sim 100\%$ , the tangential curve by  $\sim 40\%$ .

### 3.3. Numerical Example

We illustrate the analytic results obtained above using a numerically simulated galaxy cluster as a lens. It is located at redshift  $z = 0.3$  and has a mass of  $M = 5 \times 10^{14} h^{-1} M_\odot$ . The cluster was taken from a large-scale numerical simulation of the  $\Lambda$ CDM model with parameters  $\Omega_0 = 0.3$ ,  $\Omega_\Lambda = 0.7$ ,  $H_0 = 70 \text{ km s}^{-1} \text{ Mpc}^{-1}$  and normalisation  $\sigma_8 = 0.9$ . It is one of the clusters produced by the GIF collaboration (Kaldeich, 1999) used in earlier related studies (Bartelmann et al., 1998; Meneghetti et al., 2000, 2003b,a). The particle mass in the simulation is  $1.4 \times 10^{10} h^{-1} M_\odot$  and the gravitational softening length was set to  $30 h^{-1} \text{ kpc}$ .

We first use the cluster as it is, i.e. with the asymmetry and substructure produced by the simulation, and then progressively smooth and circularise it by computing its azimuthally-averaged density profile, subtracting it from the cluster, smoothing the residual density distribution by a varying amount, and finally adding the axially symmetric density profile back on the smoothed residuals. Using a normalised smoothing kernel, this procedure preserves the total mass and the mean density profile of the cluster.

Figure 5 illustrates the effect of the progressive smoothing on the critical curves. The ragged lines show the critical curve of the original clusters, while the approximately elliptical, smooth curves are the critical curves of the cluster after smoothing. Evidently, smoothing makes the critical curves shrink considerably, and, more importantly for our discussion, the radial range covered by the critical curves narrows substantially while the mean density profile remains entirely unchanged by construction. Arguments based on the cluster-centric distance of radial and tangential arcs thus need to take the detailed cluster structure into account.

## 4. SUMMARY

Galaxy clusters containing radial and tangential gravitational arcs and a brightest cluster galaxy with a measured velocity dispersion apparently require significantly flatter density profiles than obtained in numerical simulations of CDM cosmologies. As shown here, this is essentially caused by the large observed

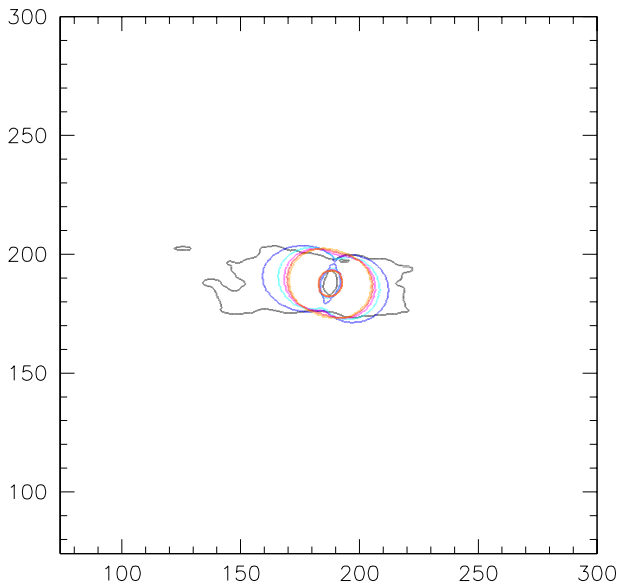


FIG. 5.—Critical curves of a simulated cluster in various stages of smoothing. As described in the text, the smoothing procedure conserves the total cluster mass and its density profile by construction. The ragged line is the original critical curve. Even moderate smoothing makes the critical curves shrink and considerably reduces the radial range where tangential and radial arcs can be found.

cluster-centric distances of tangential arcs, which require fairly flat density profiles given the central constraints of radial arcs and the velocity-dispersion measurement. Using a simple analytic mass model, we can confirm the results by STSE, *provided the lensing mass distribution is axially symmetric*.

Allowing deviations from axial symmetry, the results radically change. We have chosen to introduce asymmetry by elliptically distorting the lensing potential, but showed that embedding the axially symmetric lens into external shear has identical consequences in the limit of small ellipticity or shear. Based on these results, we have shown that the particular cluster which most significantly required a flat density profile in the analysis by STSE, Abell 383, is well compatible with an NFW profile ( $\beta = 1$ ) even for the small ellipticity of  $\epsilon = 0.1$ .

Critical curves caused by flat density profiles are extremely sensitive to distortions, as demonstrated in Sect. 3.2. and illustrated in Fig. 4. Shifting tangential critical curves by 20% to 40%, and radial critical curves by 50% to 100% even with an ellipticity or shear of only 0.1 is possible in particular for the profiles as flat as advertised by STSE. This is also the reason why the analysis of cluster ellipticity carried out by STSE themselves concluded that ellipticity had a negligible effect on their results: their lens model used components with isothermal density profiles which are much less sensitive to external shear or distortions, as illustrated by Eqs. (16) and (17).

We conclude that radial and tangential arcs in clusters do not rule out central density profiles as steep as found in CDM simulations once effects of asymmetry and shear are taken into account. We will extend our analysis towards numerically simulated clusters in a forthcoming paper.

## REFERENCES

- Bartelmann, M., Huss, A., Colberg, J., Jenkins, A., & Pearce, F. 1998, *A&A*, 330, 1  
 Jaffe, W. 1983, *MNRAS*, 202, 995  
 Jing, Y. & Suto, Y. 2000, *ApJL*, 529, L69  
 Kaldeich, B., ed. 1999, *The Next Generation Space Telescope: Science Drivers and Technological Challenges*, 34th Liège Astrophysics Colloquium (ESA)  
 Klypin, A., Kravtsov, A., Bullock, J., & Primack, J. 2001, *ApJ*, 554, 903  
 Meneghetti, M., Bartelmann, M., & Moscardini, L. 2003a, *MNRAS* submitted; preprint astro-ph/0302603  
 —. 2003b, *MNRAS*, 340, 105  
 Meneghetti, M., Bolzonella, M., Bartelmann, M., Moscardini, L., & Tormen, G. 2000, *MNRAS*, 314, 338  
 Miralda-Escudé, J. 1995, *ApJ*, 438, 514  
 Moore, B., Governato, F., Quinn, T., Stadel, J., & Lake, G. 1998, *ApJL*, 499, L5  
 Narayan, R. & Bartelmann, M. 1999, in *Formation of Structure in the Universe*, ed. A. Dekel & J. Ostriker (Cambridge: Cambridge University Press), 360  
 Navarro, J., Frenk, C., & White, S. 1997, *ApJ*, 490, 493  
 Sand, D., Treu, T., & Ellis, R. 2002, *ApJL*, 574, L129  
 Sand, D., Treu, T., Smith, G., & Ellis, R. 2003, *ApJ* submitted, preprint astro-ph/0309465  
 Schneider, P., Ehlers, J., & Falco, E. E. 1992, *Gravitational Lenses* (Springer Verlag, Heidelberg)  
 Wyithe, J., Turner, E., & Spergel, D. 2001, *ApJ*, 555, 504